# UC Irvine
## UC Irvine Previously Published Works

**Title**

Mechanistic Insights on Permeation of Water over Iron Cations in Nanoporous Silicon Oxide Films for Selective H2 and O2 Evolution

**Permalink**

https://escholarship.org/uc/item/6t46w7w2

**Journal**

ACS Applied Materials & Interfaces, 15(14)

**ISSN**

1944-8244

**Authors**

Aydin, Fikret
Andrade, Marcos F Calegari
Stinson, Robert S
et al.

**Publication Date**

2023-04-12

**DOI**

10.1021/acsami.2c22865

**Supplemental Material**

https://escholarship.org/uc/item/6t46w7w2#supplemental

**Copyright Information**

Peer reviewed

# Mechanistic Insights on Permeation of Water over Iron Cations in Nanoporous Silicon Oxide Films for Selective H₂ and O₂ Evolution

Fikret Aydin,* Marcos F. Calegari Andrade, Robert S. Stinson, Alexandra Zagalskaya,
Daniel Schwalbe-Koda, Zejie Chen, Shubham Sharma, Amitesh Maiti, Daniel V. Esposito, Shane Ardo,
Tuan Anh Pham,* and Tadashi Ogitsu*

ACCESS | Metrics & More | Article Recommendations | Supporting Information

**ABSTRACT:** Electrocatalysts encapsulated by an ultrathin and semipermeable oxide layer offer a promising avenue for efficient, selective, and cost-effective production of hydrogen through photoelectrochemical water splitting. This architecture is especially attractive for Z-scheme water splitting, for which a nanoporous oxide film can be leveraged to mitigate undesired, yet kinetically facile, reactions involving redox shuttles, such as aqueous iron cations, by limiting transport of these species to catalytically active sites. In this work, molecular dynamics simulations were combined with electrochemical measurements to provide a mechanistic understanding of permeation of water and $Fe(III)/Fe(II)$ redox shuttles through nanoporous $SiO_2$ films. It is shown that even for $SiO_2$ pores with a width as small as 0.8 nm, water does not experience any energy barrier for permeating into the pores due to a favorable interaction with hydrophilic silanol groups on the oxide surface. In contrast, permeation of $Fe(III)$ and $Fe(II)$ into microporous $SiO_2$ pores is limited due to high energy barriers, which stem from a combination of distortion and dehydration of the second and third ion solvation shells. Our simulations and experimental results show that $SiO_2$ coatings can effectively mitigate undesired $Fe(III)/Fe(II)$ redox reactions at underlying electrodes by attenuating permeation of iron cations, while allowing water to permeate and thus participate in water splitting reactions. In a broader context, our study demonstrates that selectivity of solvated cations can be manipulated by controlling the pore size and surface chemistry of oxide films.
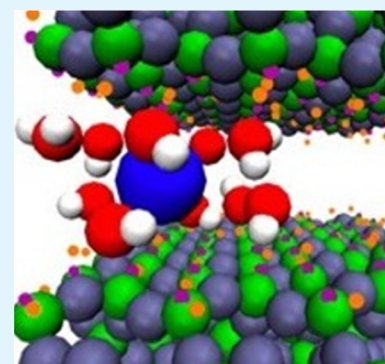
**KEYWORDS:** hydrogen production, water splitting, SiO₂ coating, selectivity of cations, molecular dynamics, metadynamics, free energy calculations, electrochemical measurements

## I. INTRODUCTION

Hydrogen production via photoelectrochemical (PEC) water splitting has long been considered a Holy Grail.[1−4] A key for the widespread deployment of this technology is the development of energy-efficient and cost-effective electrocatalysts to facilitate water splitting reactions. However, this remains a significant challenge.[5−8] Precious metals, such as Pt and Ir, have been often used to drive the two half-cell reactions in water splitting, i.e., the hydrogen evolution reaction (HER) and the oxygen evolution reaction (OER); however, they are expensive and low in availability.

In the past decades, significant efforts have been devoted toward increasing the activity of electrocatalysts for water splitting reactions by optimizing the composition and structure of their surfaces.[9−13] For example, high-throughput calculations based on density functional theory have been used to identify new binary transition-metal alloys for the HER.[9] While these studies have focused on optimizing the intrinsic properties of electrocatalyst candidates, other approaches, such as electrocatalysts encapsulated by an ultrathin and semipermeable oxide layer, provide alternative avenues for effici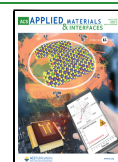ent and cost-effective hydrogen production.[14−19] Oxide encapsulation of electrocatalysts offers several advantages. The presence of an oxide layer can impart stability benefits on the electrocatalyst by mitigating dissolution and nanoparticle coalescence.[17,20] In addition, the oxide layer can be permeable to the electroactive species of interest, due to the presence of microporosity and/or interstitial free volume elements.[21−23] In this way, encapsulating oxide layers can enable selective transport of reactants and products between the bulk electrolyte and buried active electrocatalysts to manipulate chemical reactions.

Oxide-encapsulated electrocatalysts are particularly attractive for Z-scheme solar water splitting.[24,25] In this scheme, two different collections of photocatalyst particles are used to produce hydrogen and oxygen in separate reactor compart-

ments while a redox shuttle species is used to transfer charge between them, allowing for inherent product separation and mitigation of formation of an explosive gas mixture. Moreover, visible light can be utilized more efficiently than in the conventional one-step water splitting design because the energy required to drive desired reactions at each photocatalyst is reduced. However, in the Z-scheme design, the desired water splitting reactions, i.e., OER and HER, must compete with thermodynamically favorable but undesired redox shuttle reduction and oxidation reactions that limit solar-to-hydrogen conversion efficiencies. The use of oxide-encapsulated electrocatalysts can mitigate this intrinsic limitation, as the oxide overlayer can be leveraged to limit the transport of redox shuttle species to the buried electrocatalytic active sites, thereby limiting the occurrence of redox shuttle reduction and oxidation reactions (see Figure S1 for illustration). The oxide used in oxide-encapsulated electrocatalysts in this work is $SiO_2$. It is important to note some general requirements for selecting a material as an encapsulating overlayer. Besides exhibiting selective transport properties for target redox species, desirable attributes for an oxide overlayer material typically include: (i) excellent (electro)chemical stability in the chosen operating environment, (ii) high strength of adhesion to the underlying active catalyst and support material, and (iii) high electronic resistivity.[26] This last attribute can be helpful to ensure that redox reactions do not take place on the outer surface of the overlayer. Consistent with this last requirement, most oxide overlayers used for oxide-encapsulated electrocatalysts to date are wide-band-gap semiconducting or insulating materials, including but not limited to $Cr_2O_3$,[27] $SiO_2$,[28] $CeO_x$,[18] and $MnO_2$.[29]

To achieve the full benefit of oxide-encapsulated electrocatalysts for the Z-scheme design, it is essential to understand the permeation and selectivity of chemical species involved in water splitting reactions through the oxide layer. These include not only water but also redox shuttles, such as Fe(III)/Fe(II) and $IO_3^-/I^-$, which have been widely used to mediate electronic charge transfer in Z-scheme designs.[24] Although permeabilities of these species through oxides can be measured using, e.g., electroanalytical techniques,[21,22] obtaining an atomic-scale mechanistic understanding of partitioning, transport, and overall selectivity from experimental probes alone can be a significant challenge. Simulations and modeling can aid in this regard. For example, molecular dynamics (MD) simulations based on classical force fields were carried out to investigate water structure and diffusion in $SiO_2$ nanopores, and how they are influenced by the surface charge and solvated ions.[30,31] In addition, reactive all-atom MD simulations were performed to understand the structure, dynamics of water, and proton transfer at the amorphous silica surface[32] as well as to investigate the effect of confinement on water diffusion in $SiO_2$ nanopores.[33] Water structure at the interface with $SiO_2$ was also investigated by first-principles MD simulations, pointing to two unique species of adsorbed water molecules at the interface.[34,35] Last but not least, both existing experimental and computational studies suggested that water diffusion is slowed down near silanol groups.[30,36,37] Using the Clay force field and SPC/E water model, MD simulations of water-filled silica nanopores with a diameter of 1−4 nm showed that diffusion of water molecules in these systems follows a simple "core−shell" model where the first water layer is immobile, and the rest of the water molecules yield a similar diffusion coefficient as the bulk liquid.[30] We note that the SPC/E water model is known

to overestimate the diffusion coefficient of water in the bulk liquid, and a normalized diffusion coefficient was reported in this study for water in the silica pores. In support of this view, MD simulations of water-silica surfaces using ReaxFF force fields suggested that hydrogen bonds involving silanol groups are stronger than the bulk water, leading to a longer hydrogen-bond lifetime and slower water diffusion at the interface.[36] Other MD simulations also showed that diffusion coefficients of water within 6 Å from the silica surface are approximately 10 times lower than that of the bulk.[33] Consistent with these theoretical observations, experimental measurements using the Overhauser dynamic nuclear polarization technique indicated that an increase in the silanol surface density results in a slower water diffusivity.[37]

Despite a vast number of studies focusing on the effect of the silica surface on the structure and dynamics of water, permeation of redox shuttles and water from electrolytes into $SiO_2$ pores has not been studied yet. In this work, MD simulations were combined with electrochemical measurements to investigate permeation of Fe(III)/Fe(II) redox shuttle species and water through nanoporous $SiO_2$. This oxide has been experimentally demonstrated to be highly effective at suppressing undesired reactions by blocking the permeation of species, such as $Cl^-$ that participates in the undesirable chlorine evolution reaction, to the catalytically active interface, while allowing the desired reactions, such as the OER, to occur.[21,38,39] We show that water can easily permeate into nanoporous $SiO_2$ from the bulk solution, whereas both Fe(III) and Fe(II) must overcome a significantly higher energy barrier to partition into the oxide. It is found that this high energy barrier stems from a combination of desolvation and distortion of the second and third solvation shells of the cations. This behavior is in contrast to that for common monovalent cations like $Na^+$ and $K^+$, where the barrier for partitioning into subnanometer nanopores is largely due to dehydration of the first ion solvation shell.[40−43] Our simulations also demonstrate that porosity and surface chemistry can be manipulated to control permeation of desired and undesired reactions.

## II. METHODS

**A. Experimental Methods.** Nanoscopic $SiO_2$ overlayers were deposited by a room-temperature photochemical deposition process, as described in detail elsewhere.[22] First, iridium (Ir) thin-film substrates were prepared by sputtering 20 nm Ir onto fluorine-doped tin oxide (FTO)-coated glass substrates. Next, polydimethylsiloxane (PDMS) was dissolved in toluene at 5.5 mg $L^{-1}$ and spin-coated onto the Ir thin-film substrate for 2.5 min at 4000 rpm. After allowing the solvent to evaporate in an oven at 90 °C, the substrate was placed in an ultraviolet (UV) ozone cleaning system (UVOCS, T10X10/OES) for 120 min to convert the PDMS into $SiO_2$. When identical procedures were used to deposit $SiO_2$ on smooth Si wafers, the thickness of the $SiO_2$ overlayers was found to be ≈10 nm. Electrodes were also characterized by X-ray photoelectron spectroscopy (XPS) using a Physical Electronics XPS Instrument equipped with a monochromatic aluminum X-ray source and charge neutralizer. All spectra were calibrated to the C 1s peak center, which was set to 284.5 eV. Atomic ratios were calculated using atomic sensitivity factors from the Phi XPS Handbook.[44] Before electrochemical measurements, electrodes were sealed in 3M Electroplating Tape (3M) with a well-defined circular opening on the front of the electrode having an area of 0.254 $cm^2$. All current densities were calculated by dividing the measured current by this value.

Electrochemical measurements were carried out in solutions prepared from 18 MΩ-cm deionized water, $Na_2SO_4$ (ACS reagent,

≥99.0%, anhydrous, granular, Sigma Aldrich), $H_2SO_4$ (98 wt % $H_2SO_4$, Certified ACS plus, Fischer Scientific), $Fe_2(SO_4)_3$ (molecular weight 399.88 g/mol, 97%, Sigma Aldrich), and $FeSO_4$ (ACS reagent, ≥99.0%, Sigma Aldrich). Chemicals were used as received without further purification. The pH of all solutions was adjusted to a value of 1.5 through the addition of $H_2SO_4$. All solutions were degassed by purging with nitrogen gas (99.999% purity). Cyclic voltammetry (CV) measurements were carried out at room temperature (≈25 °C) in a three-neck round-bottom flask using a Ag|AgCl (saturated KCl) reference electrode and a graphite rod counter electrode. CV curves were recorded using a Biologic SP-200 potentiostat at 20 mV s$^{-1}$ for lower and upper scan vertices of 0.42 and 1.65 V vs RHE.

**B. Molecular Dynamics Simulations.** Atomistic simulations were performed to elucidate mechanisms of permeation of water and iron cations. Models of $SiO_2$ slit pores were constructed using a four-step procedure. Starting with the trigonal primitive cell of the α-quartz phase of $SiO_2$, an orthorhombic supercell consisting of 18 atoms was constructed. Next, a $7 \times 4 \times 6$ extended supercell was created, yielding a cell dimension of $24.0 \times 34.0 \times 32.4$ Å$^3$. Few layers of the oxide along the X-direction were then removed such that two planes with oxygen were exposed, which were then terminated by hydrogen atoms, and an extra vacuum was added along the X-direction (see Figure 1 for illustration). Finally, a vacuum thickness of $d$ was added
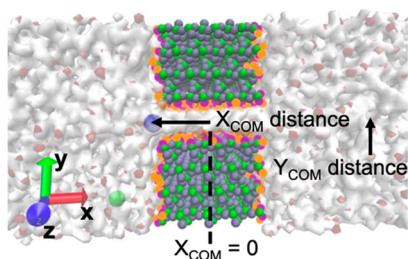


**Figure 1.** Illustration of the simulation system consisting of a $SiO_2$ nanopore wetted by an aqueous solution. The color key of the solution is red = oxygens bound to hydrogens, white = hydrogen, green = chloride, and blue = Fe(II) or Fe(III). The color key of the $SiO_2$ is gray = oxygens bound to silicon, pink = oxygens of silanol groups, orange = hydrogens of silanol groups, and green = silicon. Two collective variables, $X_{COM}$ and $Y_{COM}$, for describing permeation of a water molecule are also shown. They are defined as distances between the molecule and the center of the $SiO_2$ pore in the X and Y directions.

along the Y-direction, and the resulting free surfaces were terminated with either hydrogen for the oxygen-terminated surface or hydroxyl groups for the silicon-terminated surface. This procedure leads to a periodic orthorhombic supercell with dimensions of $111.8 \times (34.0 + d) \times 32.4$ Å$^3$, with the $SiO_2$ slit pore having a width of $d$ along the Y-direction. The final $SiO_2$ slit pore consists of 2052 atoms, with all of the silicon surface atoms terminated by hydroxyl groups. The vacuum region of the supercell was then filled with aqueous solution using the Moltemplate molecular builder.[45] Overall, the solution consists of 4317 water molecules, one redox shuttle, and an appropriate number of chlorides to achieve charge neutrality.

The simulation system was then equilibrated for 1 ns under the NPT ensemble at $T = 298.15$ K and $P = 1$ atm by using the Berendsen barostat.[46] To prevent rigid-body translation of the pore structure, we constrained silicon and oxygen atoms in the middle of the $SiO_2$ slab. All other atoms, along with surface silanol groups and liquid molecules and ions were allowed to move. In these simulations, the Lennard-Jones (LJ) parameters for Fe(III) and Fe(II) were obtained from ref 47, 48. For atoms constituting the pore structure, we used the LJ parameters provided by Joseph and Aluru.[49] A rigid SPCE water model was used in all simulations.[50]

Free energy surfaces associated with transport of the redox shuttles and water from bulk solutions into $SiO_2$ pores were then determined using well-tempered metadynamics (WT-MetaD) simulations.[51] This

approach enables sampling of rare events by depositing a history-dependent bias energy in the form of a Gaussian potential to the system's free energy landscape through a predetermined collective variable (CVs). Additional details of the WT-MetaD approach can be found in ref 51. Here, two collective variables were selected to facilitate the convergence of the PMF calculations.[52] For water, these include the center-of-mass (COM) distances between the molecule and the pore center in directions along and perpendicular to the pore entrance. For the redox shuttles, we use the distance between the ions and pore center along the pore entrance, and the number of water molecules in the first ion hydration shells. The water coordination number of the ions is described in eqs 1 and 2 to prevent discontinuities in the derivative of the CV

$$CV = \sum_{i \in A} \sum_{i \in B} s_{ij} \tag{1}$$

$$s_{ij} = \frac{1 - \left(\frac{r_{ij} - d_0}{r_0}\right)^n}{1 - \left(\frac{r_{ij} - d_0}{r_0}\right)^m} \tag{2}$$

where $s_{ij}$ quantifies a contact between atoms $i$ and $j$, $r_{ij}$ is distance between atoms, and $r_0$ is a cutoff parameter, which is set to be 0.28 and 0.26 nm for the distance between the Fe(II) and Fe(III), respectively, and the oxygen of water molecules. Other parameters including $d_0$, $n$, and $m$ were set to their default values of 0, 6, and 12, respectively. These parameters correctly capture the water coordination in the first solvation shell of the ions. It is important to note that $s_{ij}$ varies from 0 to 1, but this corresponds to only one pair of atoms, whereas the coordination CV can be larger than 1 as it includes contributions from all atoms within the cutoff distance ($CV = \sum_{i \in A} \sum_{i \in B} s_{ij}$).

WT-MetaD simulations spanning 350−450 ns were carried out to determine the free energy surfaces of redox shuttles and water through $SiO_2$ pores. In addition, four replicas of WT-MetaD simulations were carried out to enhance the statistics. The simulations were performed under the NVT ensemble at $T = 298.15$ K by using the Nose−Hoover thermostat.[53] The Gaussian bias energy is deposited every 500 steps with a height of 0.075 kJ/mol and widths of 0.65, 0.65 nm, and 0.5 for the CVs that describe $X_{COM}$, $Y_{COM}$, and water coordination number in the first ion solvation shell, respectively. The height of the Gaussian potential is tempered with a bias factor of 20. All simulations were performed using the LAMMPS package[54] patched with the PLUMED 2.5b code.[55]

## III. RESULTS AND DISCUSSION

**A. Experimental Behavior of Nanoporous $SiO_2$ Overlayers.** We begin by discussing experimental investigation of permeation of water and iron cations through nanoporous $SiO_2$. The results were obtained for $SiO_2$ overlayers deposited on Iridium (Ir) thin films, which were studied as model co-catalysts to be used on oxygen-evolving particles in Z-scheme water splitting. Cyclic voltammetry (CV) measurements were carried out in the presence and absence of Fe(III)/Fe(II) to test the effectiveness of the $SiO_2$ overlayer to selectively permit water transport while blocking transport of the iron cations. As detailed elsewhere,[22,56] ≈10 nm thick $SiO_2$ overlayers were deposited onto Ir thin-film electrodes using a photochemical deposition process. XPS characterization of an Ir control sample (Figure S2) and a $SiO_2$-encapsulated $IrO_x$ electrode shows that the presence of the overlayer almost completely screens the Ir 4f signal from the underlying Ir thin film, indicating that the $SiO_2$ overlayer continuously covers the Ir film. Previous transmission electron microscopy (TEM) characterization of $SiO_2$ overlayers made using the identical procedure showed that the overlayers are amorphous and lacked any discrete pores that could be resolved.[39]
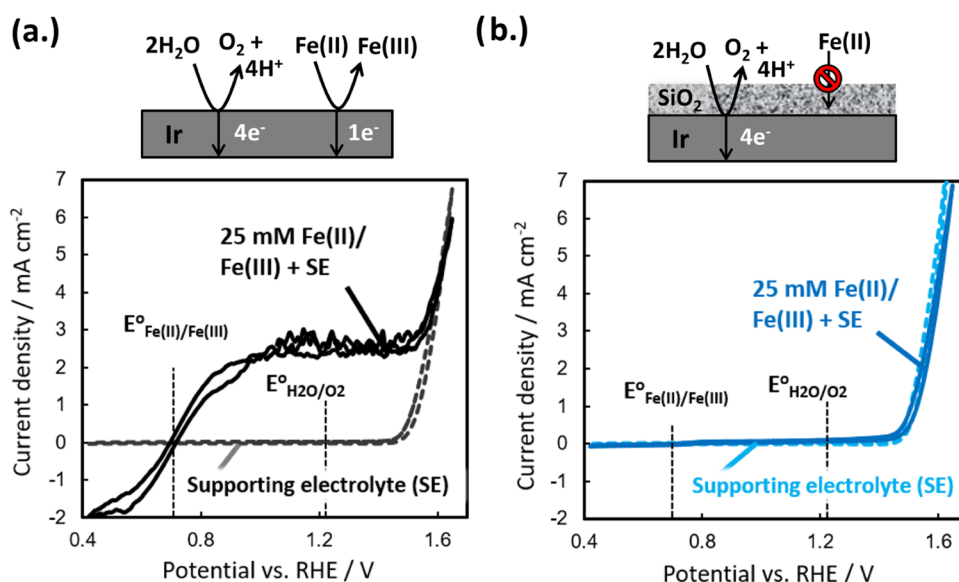
**Figure 2.** Cyclic voltammograms recorded at 20 mV s$^{-1}$ for (a) bare Ir and (b) SiO$_2$-encapsulated Ir thin film electrodes in aqueous 0.1 M Na$_2$SO$_4$ supporting electrolyte (dashed curves) and 0.1 M Na$_2$SO$_4$ + 12.5 mM Fe$_2$(SO$_4$)$_3$ + 25 mM FeSO$_4$ (solid curves). The pH of both electrolytes was adjusted to 1.5 with H$_2$SO$_4$.
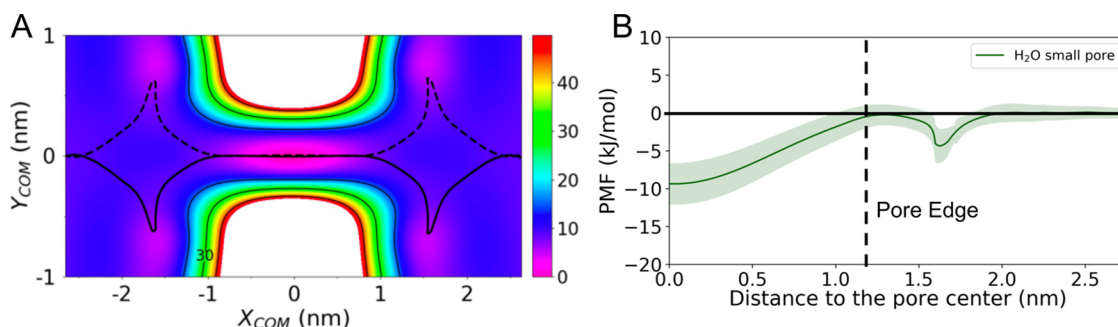


**Figure 3.** (A) Two-dimensional potential of mean force (in kJ/mol) of water permeating through a SiO$_2$ pore with a width of 0.8 nm. $X_{COM}$ and $Y_{COM}$ indicate the center-of-mass (COM) distances between water and the SiO$_2$ pore center along the pore axis and perpendicular to the pore axis, respectively. The minimum free energy path (MFEP) is represented by the black line. The value of zero kJ/mol corresponds to the lowest free energy in the 2D-PMF. (B) One-dimensional potential of mean force along the pore axis. The vertical line indicates the position of the pore entrance. The solid green line represents the average value of the PMF obtained from four individual simulations, whereas the shaded area represents the mean deviation. The energy in the bulk region was set to zero in the 1D PMFs.

The electrochemical performance of the bare Ir- and SiO$_2$-encapsulated Ir electrodes was measured in a Fe-free supporting electrolyte (0.1 M Na$_2$SO$_4$) and a Fe-containing electrolyte consisting of 25 mM Fe(II) and Fe(III) in addition to the supporting electrolyte. As shown in Figure 2 for the CV curves measured in the 0.1 M Na$_2$SO$_4$ supporting electrolyte, both electrodes exhibit an onset for the OER at ≈1.5 V vs RHE, consistent with other studies of planar Ir-based electrodes in acidic electrolytes.[57,58] Importantly, the CV curves in the supporting electrolyte are nearly identical for both electrodes, showing that the presence of the ≈10 nm SiO$_2$ overlayer has a negligible effect on the OER performance at these current densities. The results therefore suggest that water, the reactant for the OER in acidic solutions, can easily permeate through the oxide layer.

In stark contrast to the similar behavior of the two electrodes in the supporting electrolyte, Figure 2 shows that the presence of a SiO$_2$ overlayer has a drastic effect on the Fe(III)/Fe(II) redox features compared to the bare Ir electrode when CV curves were measured in the Fe-containing electrolyte. In particular, the CV curve shown in Figure 2a for the bare Ir

electrode displays significant new features associated with Fe(III) reduction and Fe(II) oxidation at potentials more negative and positive, respectively, than the reversible potential for the Fe(III)/Fe(II) redox reaction, $E°_{Fe(III)/Fe(II)}$. At overpotentials larger than ≈300 mV, both Fe(III) reduction and Fe(II) oxidation features reach a limiting current density that is associated with the maximum rate of diffusion of the reactant species across the diffusion boundary layer. On the other hand, in Figure 2b, the CV curves for the SiO$_2$|Ir electrode in the Fe-containing solution nearly overlay the CV curves measured in the supporting electrolyte, and only a small increase in oxidation signal at low current densities can be attributed to Fe(II) oxidation. Collectively, these electrochemical measurements indicate that SiO$_2$ overlayers can serve as nanoscopic membranes that selectively allow for water to pass through while blocking Fe(II) and Fe(III) species from reaching the catalytically active Ir sites at the SiO$_2$|Ir buried interface, as illustrated in Figure 2a,b.

**B. Simulating Permeation of Water and Iron Cations.** Having an initial understanding of the permeation behaviors of water and iron cations through nanoporous SiO$_2$ from
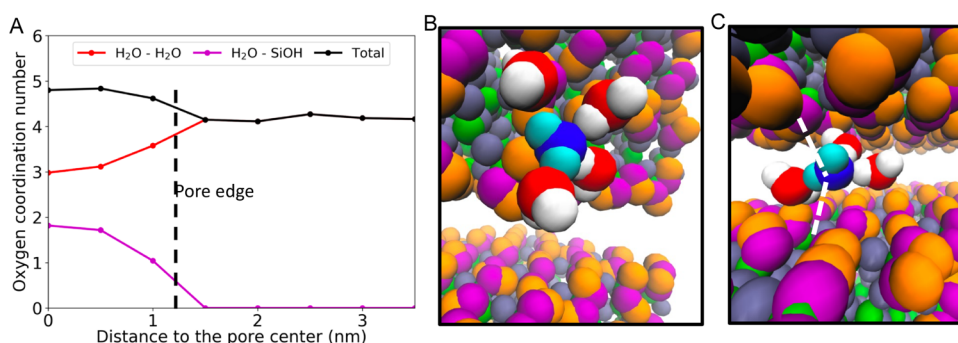
**Figure 4.** (A) Oxygen coordination number of a water molecule during transport through a small pore in $SiO_2$ with a width of 0.8 nm as a function of the distance between the water and the midpoint of the $SiO_2$ pore along the pore axis. Snapshots showing a water molecule entering the $SiO_2$ pore with its first hydration shell near the pore entrance (B) and within the pore (C). The color key is red = oxygens of water molecules, blue = oxygen of the biased water molecule in WT-MetaD simulations, white = hydrogen, gray = oxygens bound to silicon, pink = oxygens of silanol groups, orange = hydrogens of silanol groups, and green = silicon.
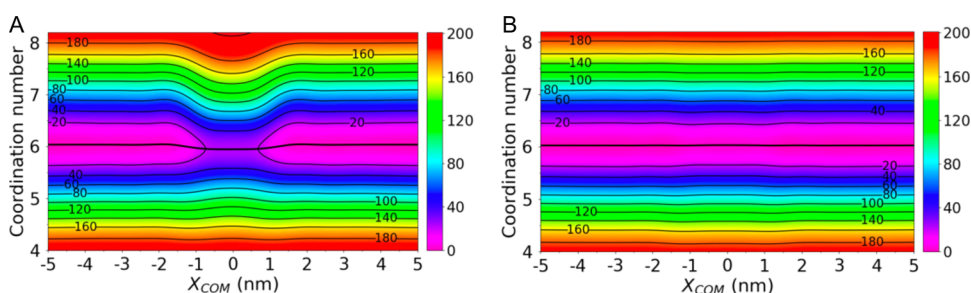


**Figure 5.** Two-dimensional potential of mean force (kJ/mol) of Fe(II) permeating through $SiO_2$ pores with a width of (A) 0.8 nm and (B) 1.2 nm. Two collective variables were used for the calculation of the PMF, including the center-of-mass distances between water and the $SiO_2$ pore center along the pore axis ($X_{COM}$) and the number of water molecules in the first ion solvation shell. Minimum free energy path (MFEP) is represented by the black line.

experiments, we then use MD simulations to investigate the permeation mechanism of these chemical species. We start with water as the reactant for water splitting reactions from bulk solutions into nanoporous $SiO_2$. Here, we consider a $SiO_2$ pore with a width of 0.8 nm that reflects median pore sizes of $SiO_2$ overlayers measured using Brunauer−Emmett−Teller analysis[15] and is consistent with ellipsometric porosimetry measurements that were not able to detect >1 nm pores.[23] Potential of mean force (PMF) associated with water transport through the oxide was then computed from WT-MetaD simulations. The PMF offers powerful means to understand transport kinetics as it provides free energy changes as a function of collective variables that are chosen to describe the state of the molecule. For water, we used two collective variables that represent the distance between the molecule and the pore center in the directions along and perpendicular to the pore entrance.

Inspection of the two-dimensional PMF (2D-PMF) shown in Figure 3A suggests that hydrophilic interactions between water and polar silanol groups of the $SiO_2$ surface play an important role in determining the water transport pathway. The calculated 2D-PMF indicates that water interacts favorably with the outer $SiO_2$ surface when approaching the pore entrance. This is also evidence in the minimum free energy path (MFEP) that represents the optimal pathway of water transport (black line, Figure 3A). Specifically, the calculated MFEP deviates significantly from a horizontal path through the pore as water molecules approach the surface. In addition, the interaction between water and surface silanol groups remains favorable as water enters the inner pore region. It is shown that

the lowest free energy region in the 2D-PMFs corresponds to the configurations where water maximizes interactions with the inner $SiO_2$ layers that are enriched with polar silanol groups. The energy barrier as a function of simulation time was also tracked to check the convergence of the individual replicas (Figure S3). It is found that the variation in the energy barrier is within 1.5 kJ/mol, which is below $k_BT$. The standard deviation across the simulations is also approximately $k_BT$, and the average PMF only slightly changes with the increasing simulation time. Our simulations also show that the biased water molecule scans all local positions within the pores, and there are multiple crossings across the small pore (Figure S4). These findings demonstrate the convergence of both individual and average PMF calculations.

To further quantify the energy barrier for water transport, it is instructive to convert the 2D-PMFs into one-dimensional PMFs along the pore axis. This 1D-PMF was obtained from the MFEP derived from the average 2D-PMFs. As expected, it is found that transport of water from bulk solution into the small $SiO_2$ pore is favorable (Figure 3B). This, again, can be attributed to favorable interactions between water molecules and silanol groups of the $SiO_2$ pore, which helps to overcome the energy penalty for breaking hydrogen bonds associated with the water molecules in the bulk solution. These findings agree with the previous experimental and computational results which demonstrate that increased interactions between water and silanol groups result in stronger hydrogen bonds compared to the bulk liquid, resulting in a longer hydrogen-bond lifetime and slower water diffusion.

These results motivated us to analyze in more detail the evolution of oxygen coordination associated with water when it enters the pore. The coordination number is calculated by averaging the oxygen coordination across the $Y$ direction for each bin along the $X$ direction. As shown in Figure 4A, water molecules recover an average oxygen coordination number of four in the bulk solution, as further illustrated in Figure 4B. Near the entrance, the oxygen coordination number to a water molecule, provided by surrounding water molecules, is reduced to three; however, the water molecule receives an additional oxygen from surface silanol groups. When the water molecule fully enters $SiO_2$, the total oxygen coordination number is increased to five, two bonds of which are contributed by surface silanol groups, as illustrated in Figure 4C. Such formation of a hydrogen-bond network between water and hydrophilic surface silanol groups compensate the energy cost for breaking hydrogen bonds around the water molecule in the bulk solution. The simulations suggest that, even for $SiO_2$ pores with a width as small as 0.8 nm, water is able to transport favorably into the oxide to participate in water splitting reactions at the interface with electrocatalysts that are buried underneath the oxide layer. These results therefore support electrochemical measurements that suggest water can permeate easily into the oxide from bulk solutions.

Here we discuss permeation of Fe(II) and Fe(III) into the same $SiO_2$ pore. For these iron cations, $X_{COM}$ and the number of water molecules in the first ion solvation shell were used as the collective variables for WT-MetaD simulations. Focusing first on Fe(II), the calculated 2D-PMF shown in Figure 5A for a small pore size of 0.8 nm suggests that the transport mechanism of Fe(II) is notably different from that of water. An important feature in the 2D-PMF of Fe(II) is a steep gradient change in the PMF as the ion approaches the pore. This indicates that permeation of Fe(II) into the pore is not favorable and that the ion experiences an energy barrier higher than that of water. WT-MetaD simulations were also carried out for Fe(II) passing through a $SiO_2$ pore with a width of 1.2 nm that represents larger pores of the oxide layer, with the resulting 2D-PMF profile shown in Figure 5B. We find that the lowest free energy region on the 2D-PMFs is largely homogeneous for the large pore, which is an indicator of a lower energy barrier for Fe(II) permeation. The same conclusions were obtained for Fe(III) (see Figure S5).

One-dimensional PFMs and associated energy barriers for transport of Fe(II) and Fe(III) into $SiO_2$ pores are summarized in Figure 6. It is shown that Fe(II) and Fe(III) experience a high energy barrier of 22 and 70 kJ/mol, respectively, for permeating into the small $SiO_2$ pore from bulk solutions. Although the energy barriers for the redox shuttles are significantly lower for the 1.2 nm pore, the barriers are much higher than that of water, yielding a value of 2 and 6 kJ/mol for Fe(II) and Fe(III), respectively. Several conclusions can be derived from these results. First, the energy barrier for transport of Fe(II) and Fe(III) is highly sensitive to the $SiO_2$ pore size. In addition, Fe(III) always experiences a higher energy barrier than Fe(II). Finally, permeation of Fe(II) and Fe(III) into $SiO_2$ is significantly limited compared to water, especially in the small pore. This is consistent with electrochemical measurements, which suggest that nanoporous $SiO_2$ coatings can suppress Fe(III) reduction and Fe(II) oxidation reactions at a catalytic interface buried underneath the oxide layer while still allowing water transport to participate in the desired HER and OER.
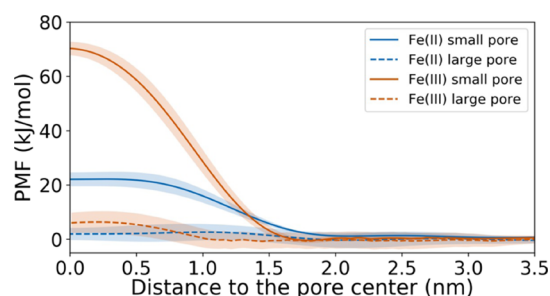


**Figure 6.** One-dimensional potential of mean force along the pore axis for transport of Fe(II) and Fe(III) from bulk solutions into nanoporous $SiO_2$. Two $SiO_2$ pores were considered, with widths of 0.8 and 1.2 nm that represent small and large pores in the oxide layer, respectively. The results were obtained from the minimum free energy paths (MFEPs) derived from the 2D-PMFs. The shaded area is the mean deviation obtained from four individual simulations.

**C. Mechanism of Ion Permeation.** Having confirmed that $SiO_2$ overlayers can selectively allow for water permeation while blocking Fe(II) and Fe(III) permeation, we used MD simulations to understand the origins of a high energy barrier for Fe(II) and Fe(III) permeation. To this end, it is instructive to investigate the solvation structures of these ions and how they vary when the ions enter the pore. This is motivated by previous studies that suggest dehydration is often a rate-limiting process that controls ion selectivity in membrane materials.[43] Here, the water coordination number in the first and second solvation shells of the ions is used as the descriptor for ion dehydration. Water oxygen-ion cutoff distances of 3.1 and 5.1 Å were used to determine the number of water molecules in the first and second solvation shells of Fe(II), respectively. Corresponding values of 3.0 and 4.8 Å were used for Fe(III). Cutoff distances were chosen as the first and second minimum of the radial distribution functions between the cations and oxygen atoms of the surrounding water molecules in the bulk solution (see Figure S6).

Results presented in Figure 7A show that the first solvation shells of both Fe(II) and Fe(III) remain intact when entering the large and small pores from the bulk solution, yielding a total of six water molecules in the first solvation shell in both bulk solution and under confinement within the pore. This indicates that unlike many monovalent ions, such as $Na^+$ and $K^+$, which have been widely investigated in the literature,[40−43] the first solvation shell of these iron cations does not easily undergo dehydration in subnanometer pores, even for pores as small as 0.8 nm. This is attributed to a strong attractive electrostatic interaction that these divalent and trivalent ions have with the surrounding water molecules, which helps them to retain all water molecules in the first solvation shells when entering the pore. Interestingly, because the first solvation shells of Fe(II) and Fe(III) are intact, these cations are not in direct contact with the oxide surfaces. This is also consistent with the observation that the 2D-PMFs of the cations are more homogeneous than that of water; for the latter, water−silanol interactions lead to local minima in the PMF of water near the edges of the pore entrance (Figure 3A). Although the first solvation shell does not undergo dehydration, its distortion might still contribute to the high energy barrier for ion permeation. To test this hypothesis, we compare the orientation distribution of water molecules in the first solvation shell of the cations in the bulk solution and under confinement. This was quantified by monitoring changes in the angle
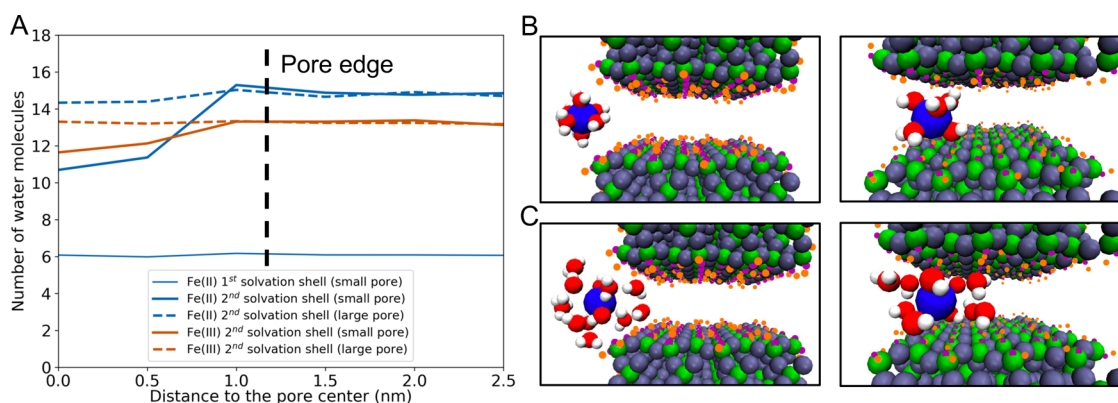
**Figure 7.** (A) Evolution of the number of water molecules in the first and second hydration shells of Fe(II) and Fe(III) as a function of the distance between the ions and $SiO_2$ pore along the pore axis for both small and large pores. (B, C) Snapshots showing the structure of the first and second solvation shells of Fe(II) in the bulk and when Fe(II) is confined in the small $SiO_2$ pore. The color key is red = oxygens of water molecules, white = hydrogen, gray = oxygens bound to silicon, pink = oxygens of silanol groups, orange = hydrogens of silanol groups, and green = silicon.
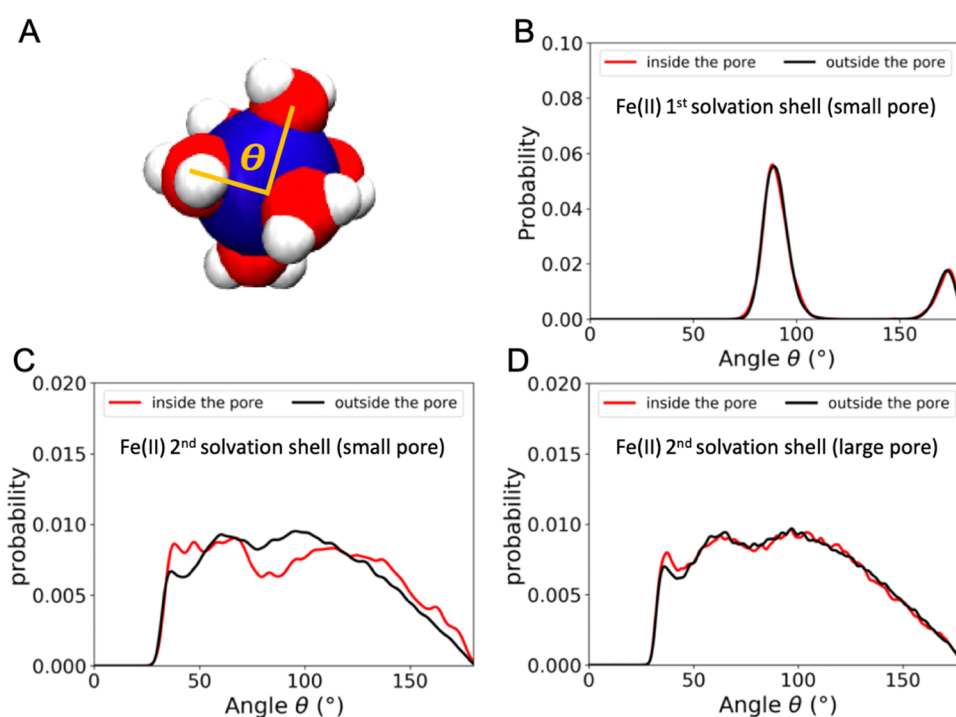


**Figure 8.** (A) Schematic of the angle describing water orientation in the first hydration shell of Fe(II). Probability distribution of angles describing the orientation of water molecules in (B) the first hydration shell and (C) the second hydration shell of Fe(II) in the small pore. (D) Result for the angle distribution of water molecules in the second hydration shell of Fe(II) in the large pore.

between vectors pointing from the cation through the oxygen atoms of surrounding water molecules, as illustrated in Figure 8A. Results in Figure 8B shows that, even for the small pore, six water molecules surrounding Fe(II) yield bond angles that are consistent with an octahedral geometry as observed in the bulk solution. In addition, little changes were found in the orientation distribution of water molecules surrounding Fe(II) between bulk and the confined system. The results indicate that the first solvation shell of Fe(II) is highly stable and rigid, e.g., the ion and first coordination sphere move as a single entity. The same conclusion was found for Fe(III) (see Figure S7). This finding implies that the energy barrier for permeation of Fe(II) and Fe(III) into oxide pores from bulk solutions is not due to dehydration or distortion of their first solvation shells.

Collectively, the analysis suggests that changes in solvation structure beyond the first solvation shell of the iron cations may be responsible for their energy barriers for entering the pores. Focusing first on the small pore, we indeed find that Fe(II) and Fe(III) lose about two to four water molecules from the second shell when entering the pore (Figure 7A). In addition, analysis of water orientation distributions also shows that the second solvation shell of the ions confined in this system is significantly distorted compared to those in the bulk solution. This is illustrated for Fe(II) in Figure 8C, and the same conclusion holds for Fe(III). These results confirm that a high energy penalty for ion permeation into the small pore can be partly attributed to a combination of distortion and partial dehydration of water molecules in the second solvation shell.

For the large pore, as expected, second solvation shells of Fe(II) and Fe(III) are less affected during transport from bulk solutions into SiO$_2$, consistent with lower energy barriers for cation transport. For example, Fe(II) loses only one water molecule in the second shell (Figure 7A), and the distribution of water orientation in this second shell is only weakly perturbed by confinement effects (Figure 8D). These observations help to explain the origins of the lower energy barrier of 2 kJ/mol for Fe(II) to transport into the large pore, compared to a value of 22 kJ/mol obtained for the small pore. Interestingly, for Fe(III), the ion retains the same number of water molecules in the second shell, while showing similar water arrangement as in the bulk solution (Figure S8). This implies that an energy barrier of 6 kJ/mol for the ion to enter the large pore should be attributed to higher-order contributions, such as partial dehydration and distortion of water in the third solvation shell.

Our results point to the importance of long-range ion−water interactions in determining the energy barrier of Fe(II) and Fe(III) transport into nanoporous SiO$_2$ that can reach beyond the first or even second solvation shells of the ions. A better understanding of this long-range interaction can be obtained by examining the PMF of a water molecule as a function of the distance from the ions. Conveniently, this can be computed as $PMF(r) = -k_B T \ln(g(r))$, where $g(r)$ is the ion−water radial distribution function obtained for bulk solutions from MD simulations. The results presented in Figure 9 show energy
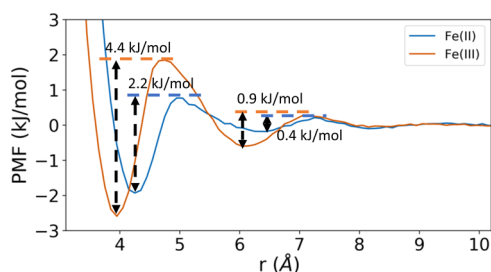


**Figure 9.** Potential of mean force (PMF) of a water molecule as a function of ion−water distance in the bulk solution. The results were derived from the ion−water radial distribution obtained from MD simulations of the bulk solution. Energy barriers to transfer a water molecule from the second and third solvation shells of Fe(II) and Fe(III) into bulk solutions are shown.

barriers of 2.2 and 4.4 kJ/mol to transfer a water molecule from the second shell of Fe(II) and Fe(III) into the bulk solution, respectively. A lower energy of 0.9 kJ/mol is required for water in the third solvation shell of Fe(III), and it is smaller for Fe(II) ($\sim$0.4 kJ/mol) due to a weaker ion−water interaction. Finally, ion−water interaction is fully screened beyond 8 Å for both ions.

Taking all of the analyses together, we conclude that, for the pore sizes considered in this work, the energy barrier for Fe(II) transport from the bulk solution into the oxide largely stems from the distortion and dehydration of water molecules in the second solvation shell. For Fe(III), the energy barrier is attributed to the same factors, but with contributions from both the second and third solvation shells due to long-range and stronger ion−water interactions. In addition, the impact of solvation shell distortion and dehydration is more pronounced in the small pore, leading to a higher energy barrier for both ions. Finally, a long-range and stronger ion−water interaction for Fe(III) also explains its higher energy barrier compared to that of Fe(II), when considering ion permeation for the same SiO$_2$ pores.

Finally, it is important to emphasize that, beyond confinement effects, chemical interactions with the pore surface species can impact the energy barrier of ion permeation. To better understand the effects of pore chemistry, energy barriers for ion permeation through SiO$_2$ were compared to those obtained for a graphene pore. In contrast to SiO$_2$, this slit pore was constructed from highly hydrophobic graphene layers. A pore size of 1.2 nm was used, which is defined as the distance between the center of mass of adjacent graphene layers. This pore size is comparable to the large SiO$_2$ pore analyzed in the previous section. The carbon atoms in graphene are described by an OPLS-AA force field,[59] while the other components are described using the same force fields used to simulate the SiO$_2$ systems.

Comparison of PMFs shows that Fe(III) ions experience higher energy barriers than Fe(II) ions for entering the graphene pore (Figure 10), e.g., the barrier is 14 and 33 kJ/mol for Fe(II) and Fe(III), respectively. This trend is consistent with the energy barriers observed for Fe(II) and Fe(III) in SiO$_2$ pores. Interestingly, the energy barrier for the ions to enter the graphene pore was found to be higher than that for SiO$_2$ with a similar pore size, e.g., Fe(II) yields a barrier of 14 and 2 kJ/mol for the graphene and SiO$_2$ pores, respectively. This indicates that although the ions do not have direct contact
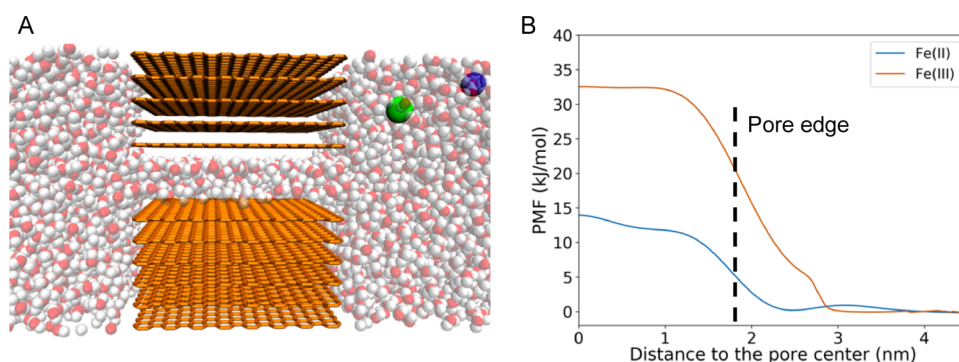


**Figure 10.** (A) Illustration of the simulation system for ion transport through a graphene pore with a width of 1.2 nm. The color key is red = oxygen of water, white = hydrogen of water, blue = Fe(II) or Fe(III), green = Cl$^-$ and orange = carbon atoms of graphene. (B) One-dimensional free energy profiles for transport of Fe(II) and Fe(III) from bulk solutions into the pore based on the minimum free energy paths (MFEPs) obtained from the 2D-PMFs.

with oxide surfaces, the hydrophilic nature of $SiO_2$ reduces the barrier for ion transport into the pore.

## IV. CONCLUSIONS

To conclude, we combined atomistic simulations and electrochemical measurements to analyze the permeation of water and Fe(II)/Fe(III) redox shuttles into 0.8 and 1.2 nm wide pores in 2 nm thick $SiO_2$ films. Our MD simulations show that, in contrast to water, which does not experience an energy barrier to enter these pores, Fe(II) and Fe(III) experience high energy barriers, especially for the smaller 0.8 nm pore. These results are supported by electrochemical measurements, suggesting that a $SiO_2$ coating can significantly attenuate Fe(III)/Fe(II) reduction at a buried electrocatalyst due to a high energy barrier for the ions to permeate into the small pores of the coating, while still allowing water transport to participate in hydrogen and oxygen evolution reactions.

This study also provides mechanistic insights into the origins of the differences in energy barriers associated with water and Fe(III)/Fe(II) entry into $SiO_2$ pores. Water does not experience any barrier for entering the pore due to a favorable interaction with hydrophilic silanol groups on the oxide surface. Conversely, both Fe(II) and Fe(III) experience significant energy barriers, which stem from a combination of distortion and dehydration of the second and/or third solvation shells. This is in contrast to common monovalent ions that have been studied in the literature, where the barrier for transport into subnanometer pores is largely due to dehydration of the first ion solvation shell. This difference in transport mechanism stems from unique long-range and strong interactions between Fe(II) and Fe(III) and surrounding water molecules. Our simulations also demonstrate that pore size and chemistry, in particular the degree of hydrophobicity, can significantly influence the barrier for ion transport. This implies that these factors can be considered for tuning species selectivity and permeability to control and improve the efficiency of hydrogen production in Z-scheme water splitting designs. In a broader context, the findings provided in this work could also be extended to other applications, such as intercalation batteries and membranes for water purification.

Finally, it is important to note that more extensive studies are needed to fully understand the physics and chemistry that underlies permeation of Fe(II)/Fe(III) redox shuttles from bulk solutions into nanoporous $SiO_2$. For example, desolvation and distortion of the first ion solvation shell may play an important role for a pore smaller than 0.8 nm. In addition, ion concentration, types of counter ions, and pH may influence not only the energy barrier but also permeation mechanism. Last but not least, a detailed understanding of transport mechanisms of other redox shuttles, such as $IO_3^-/I^-$ that has a different valency and geometry, in the oxide overlayer is also highly desirable for the development of strategies for improving the efficiency of hydrogen production in Z-scheme designs.

## ASSOCIATED CONTENT

**ⓢ Supporting Information**

The Supporting Information is available free of charge at https://pubs.acs.org/doi/10.1021/acsami.2c22865.

Detailed information regarding the computational methods and analysis (PDF)

## AUTHOR INFORMATION

**Corresponding Authors**

**Fikret Aydin** − *Materials Science Division, Lawrence Livermore National Laboratory, Livermore, California 94550, United States;* ⓞ orcid.org/0000-0003-3237-8043; Email: aydin1@llnl.gov

**Tuan Anh Pham** − *Materials Science Division, Lawrence Livermore National Laboratory, Livermore, California 94550, United States; Laboratory for Energy Applications for the Future, Lawrence Livermore National Laboratory, Livermore, California 94550, United States;* ⓞ orcid.org/0000-0003-0025-7263; Email: pham16@llnl.gov

**Tadashi Ogitsu** − *Materials Science Division, Lawrence Livermore National Laboratory, Livermore, California 94550, United States; Laboratory for Energy Applications for the Future, Lawrence Livermore National Laboratory, Livermore, California 94550, United States;* Email: ogitsu1@llnl.gov

**Authors**

**Marcos F. Calegari Andrade** − *Materials Science Division, Lawrence Livermore National Laboratory, Livermore, California 94550, United States*

**Robert S. Stinson** − *Chemical Engineering Department, Columbia Electrochemical Energy Center, Columbia University, New York, New York 10027, United States*

**Alexandra Zagalskaya** − *Materials Science Division, Lawrence Livermore National Laboratory, Livermore, California 94550, United States*

**Daniel Schwalbe-Koda** − *Materials Science Division, Lawrence Livermore National Laboratory, Livermore, California 94550, United States;* ⓞ orcid.org/0000-0001-9176-0854

**Zejie Chen** − *Department of Chemistry, University of California, Irvine, California 92697, United States*

**Shubham Sharma** − *Materials Science Division, Lawrence Livermore National Laboratory, Livermore, California 94550, United States*

**Amitesh Maiti** − *Materials Science Division, Lawrence Livermore National Laboratory, Livermore, California 94550, United States*

**Daniel V. Esposito** − *Chemical Engineering Department, Columbia Electrochemical Energy Center, Columbia University, New York, New York 10027, United States;* ⓞ orcid.org/0000-0002-0550-801X

**Shane Ardo** − *Department of Chemistry, University of California, Irvine, California 92697, United States; Department of Materials Science and Engineering and Department of Chemical and Biomolecular Engineering, University of California, Irvine, California 92697, United States;* ⓞ orcid.org/0000-0001-7162-6826

Complete contact information is available at:
https://pubs.acs.org/10.1021/acsami.2c22865

**Notes**

The authors declare no competing financial interest.

## ■ REFERENCES

(1) Grätzel, M. Photoelectrochemical cells. *Nature* **2001**, *414*, 338−344.

(2) Lewis, N. S.; Nocera, D. G. Powering the planet: chemical challenges in solar energy utilization. *Proc. Natl. Acad. Sci. U.S.A.* **2006**, *103*, 15729−15735.

(3) Walter, M. G.; Warren, E. L.; McKone, J. R.; Boettcher, S. W.; Mi, Q.; Santori, E. A.; Lewis, N. S. Solar water splitting cells. *Chem. Rev.* **2010**, *110*, 6446−6473.

(4) Pham, T. A.; Ping, Y.; Galli, G. Modelling heterogeneous interfaces for solar water splitting. *Nat. Mater.* **2017**, *16*, 401−408.

(5) Song, J.; Wei, C.; Huang, Z. F.; Liu, C.; Zeng, L.; Wang, X.; Xu, Z. J. A review on fundamentals for designing oxygen evolution electrocatalysts. *Chem. Soc. Rev.* **2020**, *49*, 2196−2214.

(6) Grimaud, A.; Diaz-Morales, O.; Han, B.; Hong, W. T.; Lee, Y. L.; Giordano, L.; Stoerzinger, K. A.; Koper, M. T. M.; Shao-Horn, Y. Activating lattice oxygen redox reactions in metal oxides to catalyse oxygen evolution. *Nat. Chem.* **2017**, *9*, 457−465.

(7) Shi, Q.; Zhu, C.; Du, D.; Lin, Y. Robust noble metal-based electrocatalysts for oxygen evolution reaction. *Chem. Soc. Rev.* **2019**, *48*, 3181−3192.

(8) Vesborg, P. C. K.; Jaramillo, T. F. Addressing the terawatt challenge: scalability in the supply of chemical elements for renewable energy. *RSC Adv.* **2012**, *2*, 7933−7947.

(9) Greeley, J.; Jaramillo, T. F.; Bonde, J.; Chorkendorff, I. B.; Norskov, J. K. Computational high-throughput screening of electro-catalytic materials for hydrogen evolution. *Nat. Mater.* **2006**, *5*, 909−913.

(10) Greeley, J.; Stephens, I. E. L.; Bondarenko, A. S.; Johansson, T. P.; Hansen, H. A.; Jaramillo, T. F.; Rossmeisl, J.; Chorkendorff, I.; Norskov, J. K. Alloys of platinum and early transition metals as oxygen reduction electrocatalysts. *Nat. Chem.* **2009**, *1*, 552−556.

(11) Seh, Z. W.; Kibsgaard, J.; Dickens, C. F.; Chorkendorff, I.; Norskov, J. K.; Jaramillo, T. F. Combining theory and experiment in electrocatalysis: Insights into materials design. *Science* **2017**, *355*, No. eaad4998.

(12) Back, S.; Tran, K.; Ulissi, Z. W. Toward a Design of Active Oxygen Evolution Catalysts: Insights from Automated Density Functional Theory Calculations and Machine Learning. *ACS Catal.* **2019**, *9*, 7651−7659.

(13) Flores, R. A.; Paolucci, C.; Winther, K. T.; Jain, A.; Torres, J. A. G.; Aykol, M.; Montoya, J.; Nørskov, J. K.; Bajdich, M.; Bligaard, T. Active Learning Accelerated Discovery of Stable Iridium Oxide Polymorphs for the Oxygen Evolution Reaction. *Chem. Mater.* **2020**, *32*, 5854−5863.

(14) Matsumori, H.; Takenaka, S.; Matsune, H.; Kishida, M. Preparation of carbon nanotube-supported Pt catalysts covered with silica layers; application to cathode catalysts for PEFC. *Appl. Catal., A* **2010**, *373*, 176−185.

(15) Takenaka, S.; Miyamoto, H.; Utsunomiya, Y.; Matsune, H.; Kishida, M. Catalytic Activity of Highly Durable Pt/CNT Catalysts Covered with Hydrophobic Silica Layers for the Oxygen Reduction Reaction in PEFCs. *J. Phys. Chem. C* **2014**, *118*, 774−783.

(16) Beatty, M. E. S.; Chen, H.; Labrador, N. Y.; Lee, B. J.; Esposito, D. V. Structure−property relationships describing the buried interface between silicon oxide overlayers and electrocatalytic platinum thin films. *J. Mater. Chem. A* **2018**, *6*, 22287−22300.

(17) Esposito, D. V. Membrane-Coated Electrocatalysts—An Alternative Approach To Achieving Stable and Tunable Electro-catalysis. *ACS Catal.* **2018**, *8*, 457−465.

(18) Speck, F. D.; Ali, F. S. M.; Paul, M. T. Y.; Singh, R. K.; Bohm, T.; Hofer, A.; Kasian, O.; Thiele, S.; Bachmann, J.; Dekel, D. R.; Kallio, T.; Cherevko, S. Improved Hydrogen Oxidation Reaction Activity and Stability of Buried Metal-Oxide Electrocatalyst Interfaces. *Chem. Mater.* **2020**, *32*, 7716−7724.

(19) Liu, Q.; Ranocchiari, M.; van Bokhoven, J. A. Catalyst overcoating engineering towards high-performance electrocatalysis. *Chem. Soc. Rev.* **2022**, *51*, 188−236.

(20) Takenaka, S.; Matsumori, H.; Nakagawa, K.; Matsune, H.; Tanabe, E.; Kishida, M. Improvement in the durability of pt electrocatalysts by coverage with silica layers. *J. Phys. Chem. C* **2007**, *111*, 15133−15136.

(21) Bhardwaj, A. A.; Vos, J. G.; Beatty, M. E. S.; Baxter, A. F.; Koper, M. T. M.; Yip, N. Y.; Esposito, D. V. Ultrathin Silicon Oxide Overlayers Enable Selective Oxygen Evolution from Acidic and Unbuffered pH-Neutral Seawater. *ACS Catal.* **2021**, *11*, 1316−1330.

(22) Beatty, M. E. S.; Gillette, E. I.; Haley, A. T.; Esposito, D. V. Controlling the Relative Fluxes of Protons and Oxygen to Electrocatalytic Buried Interfaces with Tunable Silicon Oxide Overlayers. *ACS Appl. Energy Mater.* **2020**, *3*, 12338−12350.

(23) Labrador, N. Y.; Songcuan, E. L.; De Silva, C.; Chen, H.; Kurdziel, S. J.; Ramachandran, R. K.; Detavernier, C.; Esposito, D. V. Hydrogen Evolution at the Buried Interface between Pt Thin Films and Silicon Oxide Nanomembranes. *ACS Catal.* **2018**, *8*, 1767−1778.

(24) Maeda, K. Z-Scheme Water Splitting Using Two Different Semiconductor Photocatalysts. *ACS Catal.* **2013**, *3*, 1486−1503.

(25) Wang, Y.; Suzuki, H.; Xie, J.; Tomita, O.; Martin, D. J.; Higashi, M.; Kong, D.; Abe, R.; Tang, J. Mimicking Natural Photosynthesis: Solar to Renewable H2 Fuel Synthesis by Z-Scheme Water Splitting Systems. *Chem. Rev.* **2018**, *118*, 5201−5241.

(26) Esposito, D. V.; Guilimondi, V.; Vos, J. G.; Koper, M. T. M. Chapter 7 Design Principles for Oxide-encapsulated Electrocatalysts. *Ultrathin Oxide Layers for Solar and Electrocatalytic Systems*; The Royal Society of Chemistry, 2022; pp 167−209.

(27) Maeda, K.; Teramura, K.; Lu, D.; Saito, N.; Inoue, Y.; Domen, K. Noble-metal/Cr(2)O(3) core/shell nanoparticles as a cocatalyst for photocatalytic overall water splitting. *Angew. Chem., Int. Ed.* **2006**, *45*, 7806−7809.

(28) Takenaka, S.; Matsumori, H.; Arike, T.; Matsune, H.; Kishida, M. Preparation of Carbon Nanotube-Supported Pt Metal Particles Covered with Silica Layers and Their Application to Electrocatalysts for PEMFC. *Top. Catal.* **2009**, *52*, 731−738.

(29) Vos, J. G.; Wezendonk, T. A.; Jeremiasse, A. W.; Koper, M. T. M. MnO(x)/IrO(x) as Selective Oxygen Evolution Electrocatalyst in Acidic Chloride Solution. *J. Am. Chem. Soc.* **2018**, *140*, 10270−10281.

(30) Bourg, I. C.; Steefel, C. I. Molecular Dynamics Simulations of Water Structure and Diffusion in Silica Nanopores. *J. Phys. Chem. C* **2012**, *116*, 11556−11564.

(31) Collin, M.; Gin, S.; Dazas, B.; Mahadevan, T.; Du, J.; Bourg, I. C. Molecular Dynamics Simulations of Water Structure and Diffusion in a 1 nm Diameter Silica Nanopore as a Function of Surface Charge and Alkali Metal Counterion Identity. *J. Phys. Chem. C* **2018**, *122*, 17764−17776.

(32) Lentz, J.; Garofalini, S. H. Role of the hydrogen bond lifetimes and rotations at the water/amorphous silica interface on proton transport. *Phys. Chem. Chem. Phys.* **2019**, *21*, 12265−12278.

(33) Xu, S.; Simmons, G. C.; Mahadevan, T. S.; Scherer, G. W.; Garofalini, S. H.; Pacheco, C. Transport of water in small pores. *Langmuir* **2009**, *25*, 5084−5090.

(34) Gaigeot, M. P.; Sprik, M.; Sulpizi, M. Oxide/water interfaces: how the surface chemistry modifies interfacial water properties. *J. Phys.: Condens. Matter* **2012**, *24*, No. 124106.

(35) Sulpizi, M.; Gaigeot, M. P.; Sprik, M. The Silica-Water Interface: How the Silanols Determine the Surface Acidity and

Modulate the Water Properties. *J. Chem. Theory Comput.* **2012**, *8*, 1037−1047.

(36) Mizuguchi, T.; Hagita, K.; Fujiwara, S.; Yamada, T. Hydrogen bond analysis of confined water in mesoporous silica using the reactive force field. *Mol. Simul.* **2019**, *45*, 1437−1446.

(37) Schrader, A. M.; Monroe, J. I.; Sheil, R.; Dobbs, H. A.; Keller, T. J.; Li, Y.; Jain, S.; Shell, M. S.; Israelachvili, J. N.; Han, S. Surface chemical heterogeneity modulates silica surface hydration. *Proc. Natl. Acad. Sci. U.S.A.* **2018**, *115*, 2890−2895.

(38) Fabian, D. M.; Hu, S.; Singh, N.; Houle, F. A.; Hisatomi, T.; Domen, K.; Osterlohf, F. E.; Ardo, S. Particle suspension reactors and materials for solar-driven water splitting. *Energy Environ. Sci.* **2015**, *8*, 2825−2850.

(39) Labrador, N. Y.; Li, X.; Liu, Y.; Tan, H.; Wang, R.; Koberstein, J. T.; Moffat, T. P.; Esposito, D. V. Enhanced Performance of Si MIS Photocathodes Containing Oxide-Coated Nanoparticle Electrocatalysts. *Nano Lett.* **2016**, *16*, 6452−6459.

(40) Aydin, F.; Moradzadeh, A.; Bilodeau, C. L.; Lau, E. Y.; Schwegler, E.; Aluru, N. R.; Pham, T. A. Ion Solvation and Transport in Narrow Carbon Nanotubes: Effects of Polarizability, Cation-pi Interaction, and Confinement. *J. Chem. Theory Comput.* **2021**, *17*, 1596−1605.

(41) Li, Z.; Li, Y.; Yao, Y. C.; Aydin, F.; Zhan, C.; Chen, Y.; Elimelech, M.; Pham, T. A.; Noy, A. Strong Differential Monovalent Anion Selectivity in Narrow Diameter Carbon Nanotube Porins. *ACS Nano* **2020**, *14*, 6269−6275.

(42) Zhan, C.; Aydin, F.; Schwegler, E.; Noy, A.; Pham, T. A. Understanding Cation Selectivity in Carbon Nanopores with Hybrid First-Principles/Continuum Simulations: Implications for Water Desalination and Separation Technologies. *ACS Appl. Nano Mater.* **2020**, *3*, 9740−9748.

(43) Faucher, S.; Aluru, N.; Bazant, M. Z.; Blankschtein, D.; Brozena, A. H.; Cumings, J.; de Souza, J. P.; Elimelech, M.; Epsztein, R.; Fourkas, J. T.; Rajan, A. G.; Kulik, H. J.; Levy, A.; Majumdar, A.; Martin, C.; McEldrew, M.; Misra, R. P.; Noy, A.; Pham, T. A.; Reed, M.; Schwegler, E.; Siwy, Z.; Wang, Y. H.; Strano, M. Critical Knowledge Gaps in Mass Transport through Single-Digit Nanopores: A Review and Perspective. *J. Phys. Chem. C* **2019**, *123*, 21309−21326.

(44) Moulder, S. F.; Stickle, W. F.; Sobol, W. M.; Bomben, K. D. Handbook of X-Ray Photoelectron Spectroscopy; 1992.

(45) Jewett, A. I.; Stelter, D.; Lambert, J.; Saladi, S. M.; Roscioni, O. M.; Ricci, M.; Autin, L.; Maritan, M.; Bashusqeh, S. M.; Keyes, T.; Dame, R. T.; Shea, J. E.; Jensen, G. J.; Goodsell, D. S. Moltemplate: A Tool for Coarse-Grained Modeling of Complex Biological Matter and Soft Condensed Matter Physics. *J. Mol. Biol.* **2021**, *433*, No. 166841.

(46) Berendsen, H. J. C.; Postma, J. P. M.; van Gunsteren, W. F.; DiNola, A.; Haak, J. R. Molecular dynamics with coupling to an external bath. *J. Chem. Phys.* **1984**, *81*, 3684−3690.

(47) Li, P.; Roberts, B. P.; Chakravorty, D. K.; Merz, K. M., Jr. Rational Design of Particle Mesh Ewald Compatible Lennard-Jones Parameters for +2 Metal Cations in Explicit Solvent. *J. Chem. Theory Comput.* **2013**, *9*, 2733−2748.

(48) Li, P.; Song, L. F.; Merz, K. M., Jr. Parameterization of highly charged metal ions using the 12-6-4 LJ-type nonbonded model in explicit water. *J. Phys. Chem. B* **2015**, *119*, 883−895.

(49) Joseph, S.; Aluru, N. R. Hierarchical multiscale simulation of electrokinetic transport in silica nanochannels at the point of zero charge. *Langmuir* **2006**, *22*, 9041−9051.

(50) Berendsen, H. J. C.; Grigera, J. R.; Straatsma, T. P. The missing term in effective pair potentials. *J. Phys. Chem. A* **1987**, *91*, 6269−6271.

(51) Barducci, A.; Bussi, G.; Parrinello, M. Well-tempered metadynamics: a smoothly converging and tunable free-energy method. *Phys. Rev. Lett.* **2008**, *100*, No. 020603.

(52) Aydin, F.; Sun, R.; Swanson, J. M. J. Mycolactone Toxin Membrane Permeation: Atomistic versus Coarse-Grained MARTINI Simulations. *Biophys. J.* **2019**, *117*, 87−98.

(53) Nosé, S. A unified formulation of the constant temperature molecular dynamics methods. *J. Chem. Phys.* **1984**, *81*, 511−519.

(54) Plimpton, S. Fast Parallel Algorithms for Short-Range Molecular-Dynamics. *J. Comput. Phys.* **1995**, *117*, 1−19.

(55) Tribello, G. A.; Bonomi, M.; Branduardi, D.; Camilloni, C.; Bussi, G. PLUMED 2: New feathers for an old bird. *Comput. Phys. Commun.* **2014**, *185*, 604−613.

(56) Mirley, C. L.; Koberstein, J. T. A Room Temperature Method for the Preparation of Ultrathin SiOx Films from Langmuir-Blodgett Layers. *Langmuir* **1995**, *11*, 1049−1052.

(57) Reier, T.; Oezaslan, M.; Strasser, P. Electrocatalytic Oxygen Evolution Reaction (OER) on Ru, Ir, and Pt Catalysts: A Comparative Study of Nanoparticles and Bulk Materials. *ACS Catal.* **2012**, *2*, 1765−1772.

(58) Ahn, S. H.; Tan, H.; Haensch, M.; Liu, Y.; Bendersky, L. A.; Moffat, T. P. Self-terminated electrodeposition of iridium electrocatalysts. *Energy Environ. Sci.* **2015**, *8*, 3557−3562.

(59) Jorgensen, W. L.; Maxwell, D. S.; TiradoRives, J. Development and testing of the OPLS all-atom force field on conformational energetics and properties of organic liquids. *J. Am. Chem. Soc.* **1996**, *118*, 11225−11236.